Electronic Supplementary Material (ESI) for Nanoscale.

Supporting Information

Giant in-plane optical and electronic anisotropy in tellurene：A quantitative exploration

Zhengfeng Guo,[ab] *Honggang Gu,*[*ad] *Mingsheng Fang,* [a] *Lei Ye*[c] *and Shiyuan Liu*[*acd]

[a]*State Key Laboratory of Digital Manufacturing Equipment and Technology, Huazhong University of Science and Technology, Wuhan 430074, China*

[b]*Innovation Institute, Huazhong University of Science and Technology, Wuhan 430074, China*

[c]*School of Optical and Electronic Information, Huazhong University of Science and Technology, Wuhan 430074, China*

[d]*Optics Valley Laboratory, Wuhan 430074, China*

[*]Corresponding E-mails:
hongganggu@hust.edu.cn (H. Gu); shyliu@hust.edu.cn (S. Liu).

Supporting Note S1. Theoretical calculating peak intensities of the Raman modes

The theoretical peak intensities of the Raman modes are calculated to fit the experimental ones. The peak intensity I of each Raman mode can be calculated by the formula[S1, 2]

$$I \propto \left|\mathbf{e}_{\text{out}} \cdot \mathbf{R} \cdot \mathbf{e}_{\text{in}}\right|^2, \tag{S1}$$

where, $\mathbf{e}_{\text{out}}$ and $\mathbf{e}_{\text{in}}$ are respectively the unit polarization vectors of the scattered Raman signal and the incident laser. After the incident laser goes through the polarizer, its electric field direction is parallel to the z-axis of the Raman laboratory coordinates, and $\mathbf{e}_{\text{in}} = [0, 0, 1]^{\text{T}}$. Since the analyzer is parallel to the polarizer (Fig. S3), we have $\mathbf{e}_{\text{out}} = [0, 0, 1]$. $\mathbf{R}$ is the Raman tensor for each Raman mode. Tellurene belongs to the D_3^4 space group[S3], and therefore the Raman tensors for A_1, E_1-TO, and E_2 are respectively given by[S4]

$$\mathbf{R}_{\text{A}_1} = \begin{bmatrix} a & 0 & 0 \\ 0 & a & 0 \\ 0 & 0 & b \end{bmatrix}, \tag{S2a}$$

$$\mathbf{R}_{\text{E}_1\text{-TO}} = \begin{bmatrix} c & 0 & 0 \\ 0 & -c & d \\ 0 & d & 0 \end{bmatrix}, \tag{S2b}$$

and

$$\mathbf{R}_{\text{E}_2} = \begin{bmatrix} 0 & -c & -d \\ -c & 0 & 0 \\ -d & 0 & 0 \end{bmatrix}. \tag{S2c}$$

The Raman tensors are defined with respect to the crystal coordinates. Therefore, the coordinate conversion must be taken into account due to the azimuth rotation of the sample in the Raman measurements. The Raman tensors after the coordinate conversion $\mathbf{R}'$ can be written as[S1]

$$\mathbf{R}' = \mathbf{A}^{\text{T}}\mathbf{R}\mathbf{A}, \tag{S3a}$$

where, $\mathbf{A}$ is the rotation matrix

$$\mathbf{A}=\begin{bmatrix}\cos(\theta+\alpha) & 0 & \sin(\theta+\alpha)\\ 0 & 1 & 0\\ -\sin(\theta+\alpha) & 0 & \cos(\theta+\alpha)\end{bmatrix}, \tag{S3b}$$

and $\mathbf{A}^{\mathrm{T}}$ is the transposed matrix of **A**. Herein, θ is the angle between the *z*-axis and the *c*-axis of the tellurene nanosheet, and α is the rotation angle, as shown in Fig. S4.

According to the above derivation, the peak intensity of the Raman mode in our measurement configuration can be described as

$$I \propto \left|\mathbf{e}_{\mathrm{out}}\cdot\mathbf{R}'\cdot\mathbf{e}_{\mathrm{in}}\right|^2=\left|\mathbf{e}_{\mathrm{out}}\cdot\mathbf{A}^{\mathrm{T}}\mathbf{R}\mathbf{A}\cdot\mathbf{e}_{\mathrm{in}}\right|^2. \tag{S4a}$$

Ultimately, the peak intensities of A_1, E_1-TO, and E_2 Raman modes are respectively given by

$$I_{\mathrm{A_1}} \propto \left|a\sin^2(\theta+\alpha)+b\cos^2(\theta+\alpha)\right|^2, \tag{S4b}$$

$$I_{\mathrm{E_1\text{-}TO}} \propto \left|c\sin^2(\theta+\alpha)\right|^2, \tag{S4c}$$

and

$$I_{\mathrm{E_2}} \propto \left|-2d\sin(\theta+\alpha)\cos(\theta+\alpha)\right|^2=\left|d\sin 2(\theta+\alpha)\right|^2. \tag{S4e}$$

Here, θ is 90°, which means z-axis and c-axis is perpendicular to each other at the initial Raman measurement.

Supporting Note S2. Imaging Mueller matrix spectroscopic ellipsometry analysis

The constructed stacking model is composed of the geometric structure and the dielectric function for each part of geometric construction. The tellurene nanosheet and Si substrate with SiO_2 oxide layer consist of the multilayer film structure. The structure parameters for this multilayer film structure are the thickness of each layer. Besides, on account of smooth surface of tellurene nanosheet measured by AFM in Fig. S7, the roughness of tellurene nanosheet or overlay model (such as effective medium approximation, EMA[S5]) are not taken into consideration. Since more attention is paid to the layer of tellurene nanosheet, the thickness and the dielectric function of Si substrate with SiO_2 oxide layer were predetermined with a separate reference measurement on an uncoated region before determining those of tellurene nanosheet.

To acquire the thickness and the dielectric function of tellurene nanosheet, the cubic-

spline functions[S6] vertical and parallel to the optics axis were applied and adjusted to obtain the best match with experimental data. Owing to the fact that the cubic-spline functions are not satisfied with Kramers-Kronig consistency[S7], the cubic-spline functions are lack of direct physical meaning. In consequence, the Lorentz oscillator model (with physical implication) along and vertical to the optics axis was introduced to fit Mueller matrix spectra, which is expressed as the sum form of several Lorentz oscillators[S8, 9]

$$\varepsilon(E) = \sum_{q}^{Q} \varepsilon_{\text{Lorentz}}^{q}(E_{0,q},\ A_q,\ \Gamma_q; E) = \sum_{q}^{Q} \frac{E_{0,q} A_q}{E_{0,q}^2 - E^2 + \mathrm{i}\Gamma_q E}. \tag{S5}$$

In Equation S1, E is the photon energy with the unit of eV, and the Q is the total number of Lorentz oscillators. In addition, $E_{0,q}$, A_q, and Γ_q are the qth oscillator's center energy, strength (amplitude), and damping coefficient respectively.

In our ellipsometric analysis, both two Lorentz oscillators were employed along and vertical to the optics axis, whose best fitted parameters are summarized in Table S1.

Besides, the extracted thickness of the tellurene nanosheet is 71.0 nm in perfect accordance with the AFM value 72.6 nm as shown in Fig. S6, further implying the reliability and accuracy of the ellipsometric analysis.

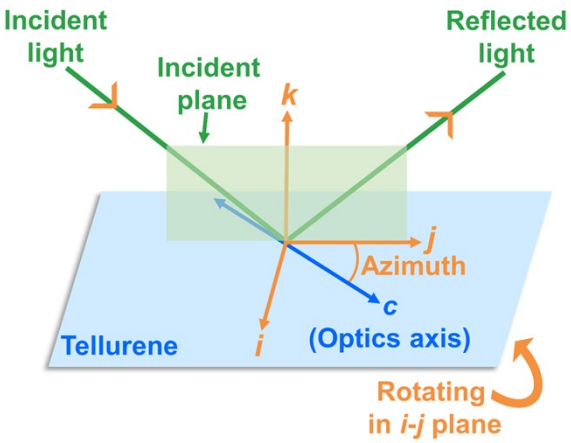

Fig. S1 The ellipsometric measurement schematic diagram of tellurium (Te), where the azimuth is defined as the angle between *c*-axis of Te and *j*-axis of ellipsometric coordinate (*i*-*j*-*k*).

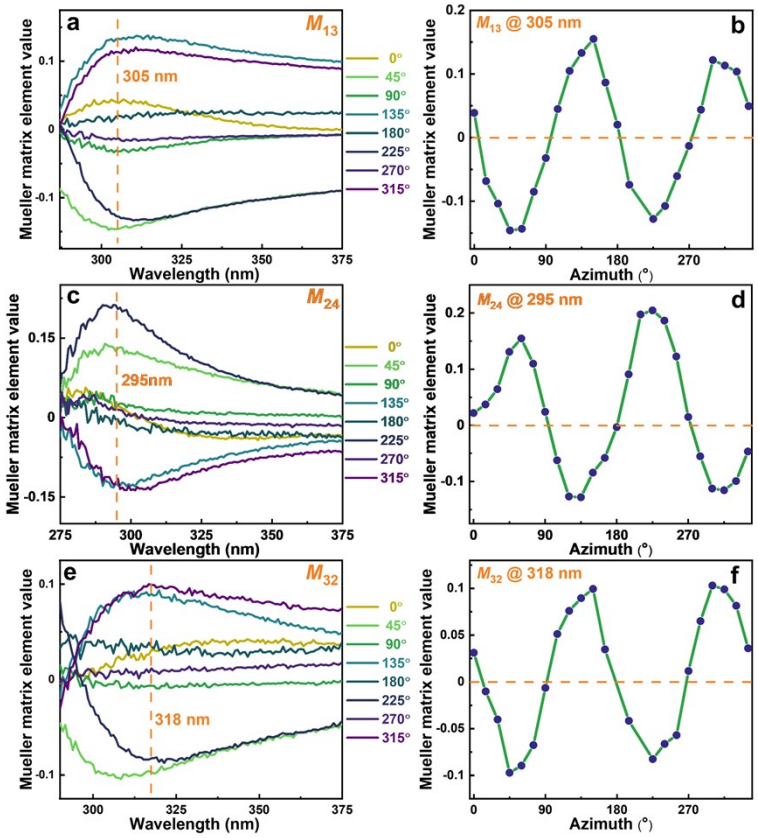

Fig. S2 The other representative azimuth-sensitive off-diagonal Mueller matrix elements (M_{13}, M_{24}, and M_{32}) spectra at varied azimuths and incident angle θ_i of 65° (**a, c, and e**) and those at the selected wavelength (**b, d, and f**).

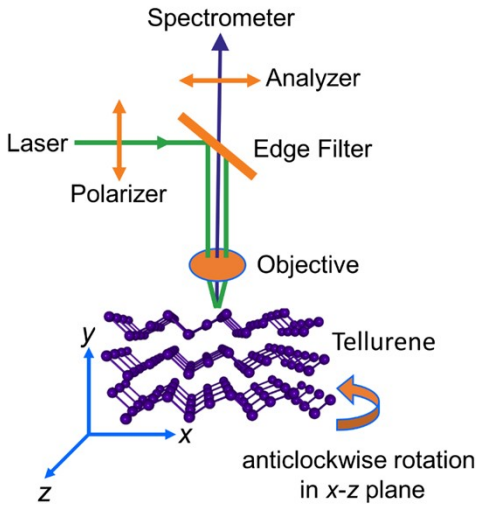

Fig. S3 Schematic diagram of the Raman system configuration, where the polarizer and analyzer are parallel to each other and the tellurene is anticlockwise rotated in *x*-*z* plane.

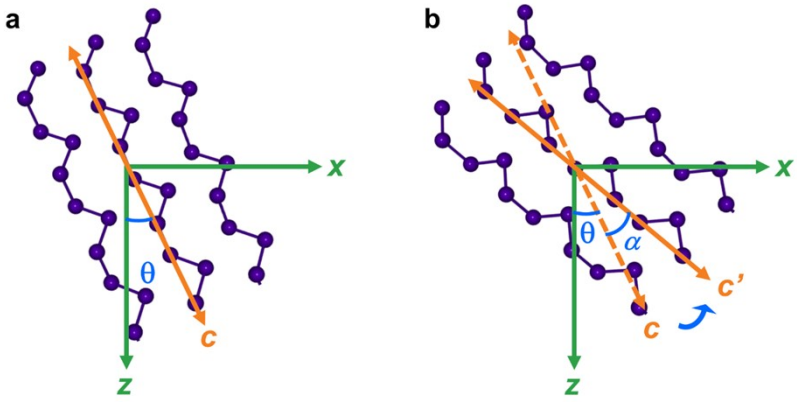

Fig. S4 The tellurene in *x*-*z* plane of Raman coordinate (*x*–*y*–*z*) at the beginning of Raman measurement (**a**) and after anticlockwise rotating α° (**b**).

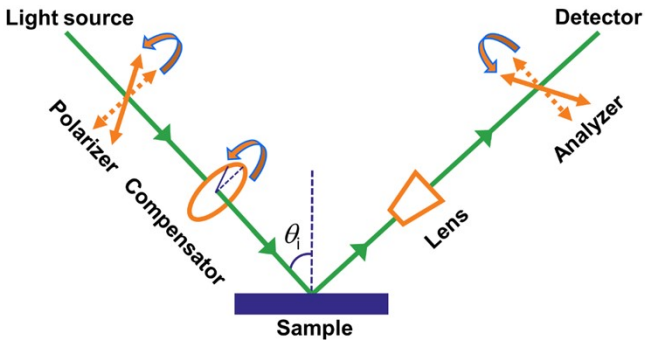

Fig. S5 The working principle of the imaging Mueller matrix spectroscopic ellipsometry (MMSE), where θ_i represents the incident angle and the polarizer, compensator and analyzer are rotatable to obtain the first three row of Mueller matrix and high spatial contrast of sample[S8, 10]. Combined with microscopic imaging system,

the lateral resolution of the imaging MMSE can even reach up to 2 μm[S6].

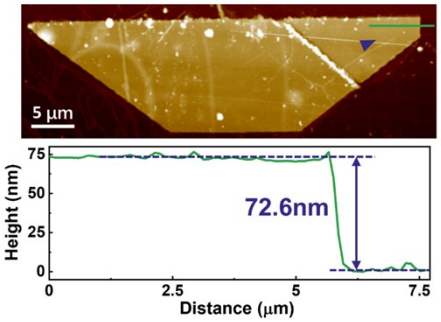

Fig. S6 The atomic force microscopy (AFM) image of the same tellurene nanosheet measured by the imaging MMSE, where the triangle is the region to extract the Mueller matrix spectra for the spectroscopic analysis.

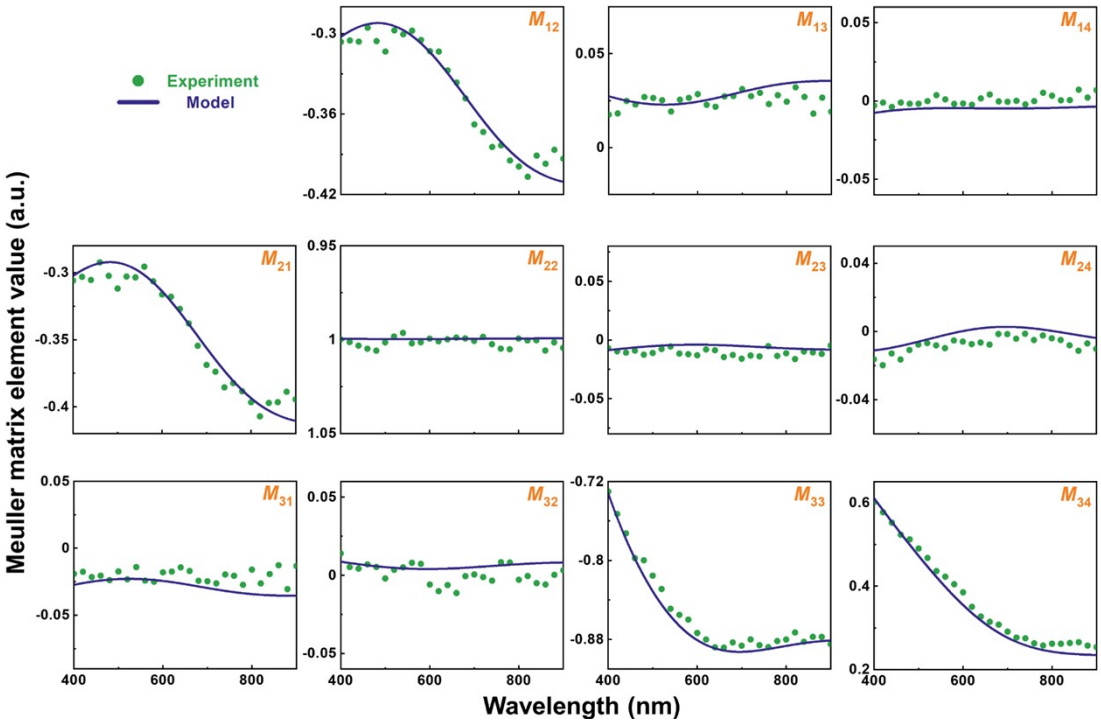

Fig. S7 The experimental (green points) and model-calculated (solid line) Mueller matrix spectra at the incident angle of 50°.

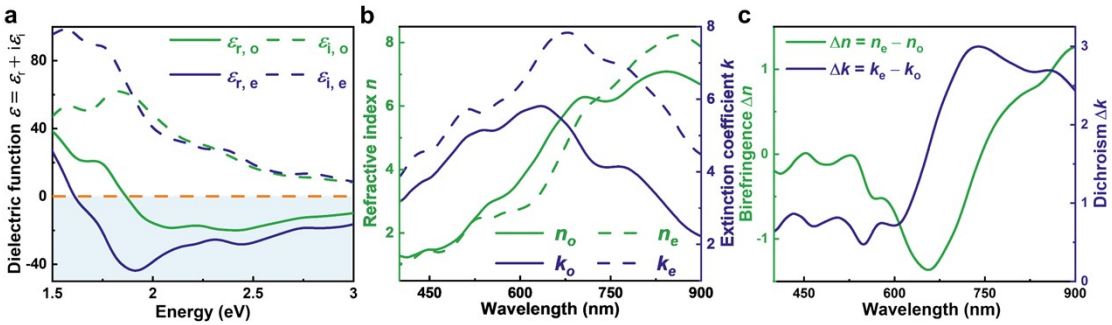

Fig. S8 The first-principle calculated dielectric function spectra (a), complex refractive index spectra (b), and in-plane birefringence Δn (= $n_e - n_o$) and dichroism Δk (= $k_e - k_o$).

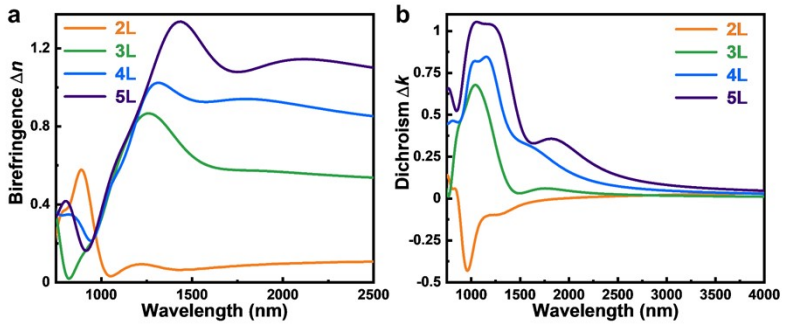

Fig. S9 The first-principle calculated tellurene's thickness dependence of birefringence Δn (a) and dichroism Δk (b), where "L" denotes layers.

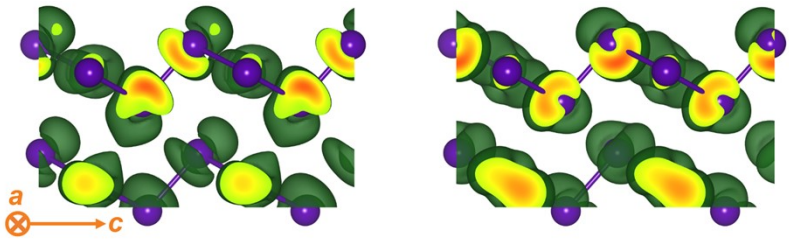

Fig. S10 The charge density of conduction band maximum (CBM) using an isosurface of 0.3 meÅ^{-3}, left: along the *a*-axis, right: along the *c*-axis

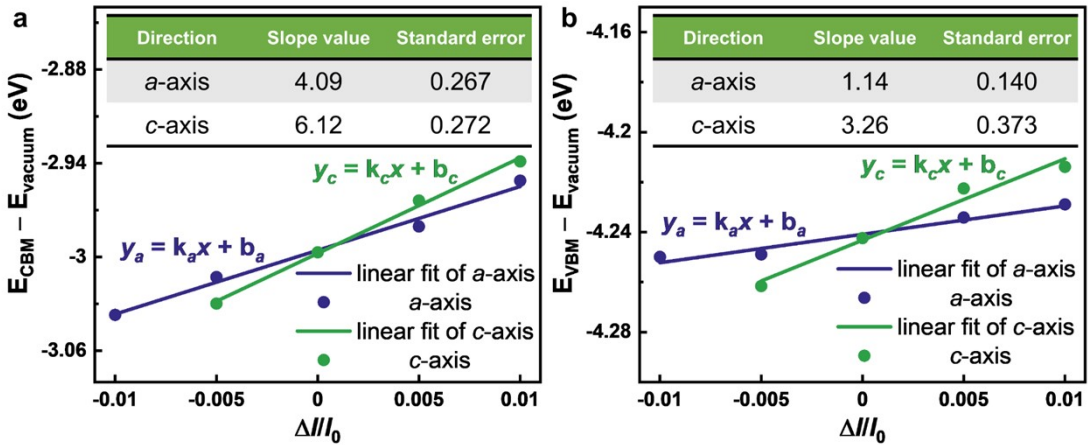

Fig. S11 The relationship between conduction band minimum (CBM, **a**) or valence band maximum (VBM, **b**), deducting the vacuum energy level E_{vacuum}, and deformation of lattice constant (*a*-axis or *c*-axis) $\Delta l_j / l_{0,j}\ (j = a, c)$ with their linearly fit, where the insert tables are the slopes and its standard errors of these linearly fitted lines. As -0.01 strain (compressive strain) along *c*-axis causes great fluctuation in linearly fitting, it is excluded from linearly fit.

Table S1. The best fitted parameters of Lorentz oscillators model used in uniaxial anisotropic model of tellurene nanosheet.

	Center energy (E_0) [eV]	Amplitude (A) [(eV)^2]	Damping coefficient (Γ) [eV]
ε_o	1.10 ± 0.172	33.84 ± 16.178	1.59 ± 0.152
	1.61 ± 0.060	36.26 ± 15.737	1.36 ± 0.127
ε_e	1.08 ± 0.221	51.38 ± 2.724	5.79 ± 0.775
	1.85 ± 0.007	29.76 ± 1.970	1.22 ± 0.039

Table S2. Comparison of birefringence in commercial birefringent materials, typical low-dimensional materials, and well-designed birefringent materials.

Materials	Birefringence (Δn)	References
Tellurene	0.48	This work
Quartz (SiO_2)	0.009	Ref S11
MgF_2	0.012	Ref S12
Calcite ($CaCO_3$)	0.20	Ref S11
Black phosphorus (BP)	0.15	Ref S13
TiS_3	0.30 ±0.04	Ref S14
$BaTiS_3$	0.76	Ref S15
h-BN[a]	0.3 in vis-near infrared region 2 in UV region	Ref S16, 17
α-MoO_3	0.11	Ref S18
MoS_2[a]	1.5 in near infrared region 3 in visible range	Ref S19
Cs_4PbBr_6 perovskite crystals embedded with $CsPbBr_3$ nanocrystals	0.018	Ref S20
$CeF_2(SO_4)$	0.36	Ref S21
$Rb_2VO(O_2)_2F$	0.19	Ref S22
$[Al(H_2O)_6](IO_3)_2(NO_3)$	0.252	Ref S23

[a] although the birefringences of h-BN and MoS_2 are rather larger than many other materials, they are out-of-plane rather than more accessible in-plane birefringence like tellurene.

References

S1. X.-L. Liu, X. Zhang, M.-L. Lin and P.-H. Tan, *Chin. Phys. B*, 2017, **26**, 067802.

S2. M. A. Pimenta, G. C. Resende, H. B. Ribeiro and B. R. Carvalho, *Phys. Chem. Chem. Phys.*, 2021, **23**, 27103-27123.

S3. L. Tong, X. Huang, P. Wang, L. Ye, M. Peng, L. An, Q. Sun, Y. Zhang, G. Yang, Z. Li, F. Zhong, F. Wang, Y. Wang, M. Motlag, W. Wu, G. J. Cheng and W. Hu, *Nat. Commun.*, 2020, **11**, 2308.

S4. E. Anastassakis and M. Cardona, *Phys. Status Solidi B*, 1981, **104**, 589-600.

S5. P. Petrik, M. Fried, T. Lohner, R. Berger, L. P. Bíró, C. Schneider, J. Gyulai and H. Ryssel, *Thin Solid Films*, 1998, **313-314**, 259-263.

S6. S. Funke, M. Duwe, F. Balzer, P. H. Thiesen, K. Hingerl and M. Schiek, *J. Phys. Chem. Lett.*, 2021, **12**, 3053-3058.

S7. B. Su, Y. Song, Y. Hou, X. Chen, J. Zhao, Y. Ma, Y. Yang, J. Guo, J. Luo and Z.-G. Chen, *Adv. Mater.*, 2019, **31**, 1903498.

S8. H. Fujiwara, *Spectroscopic ellipsometry: principles and applications*, John Wiley & Sons, Chichester, England, 2007.

S9. Z. Guo, H. Gu, M. Fang, B. Song, W. Wang, X. Chen, C. Zhang, H. Jiang, L. Wang and S. Liu, *ACS Mater. Lett.*, 2021, **3**, 525-534.

S10. P. S. Hauge, *Surf. Sci.*, 1980, **96**, 108-140.

S11. G. Ghosh, *Opt. Commun.*, 1999, **163**, 95-102.

S12. M. J. Dodge, *Appl. Opt.*, 1984, **23**, 1980-1985.

S13. S.-Y. Lee and K.-J. Yee, *2D Mater.*, 2021, **9**, 015020.

S14. N. Papadopoulos, R. Frisenda, R. Biele, E. Flores, J. R. Ares, C. Sánchez, H. S. J. van der Zant, I. J. Ferrer, R. D'Agosta and A. Castellanos-Gomez, *Nanoscale*, 2018, **10**, 12424-12429.

S15. S. Niu, G. Joe, H. Zhao, Y. Zhou, T. Orvis, H. Huyan, J. Salman, K. Mahalingam, B. Urwin, J. Wu, Y. Liu, T. E. Tiwald, S. B. Cronin, B. M. Howe, M. Mecklenburg, R. Haiges, D. J. Singh, H. Wang, M. A. Kats and J. Ravichandran, *Nat. Photonics*, 2018, **12**, 392-396.

S16. Y. Rah, Y. Jin, S. Kim and K. Yu, *Opt. Lett.*, 2019, **44**, 3797-3800.

S17. A. Segura, L. Artús, R. Cuscó, T. Taniguchi, G. Cassabois and B. Gil, *Phys. Rev. Mater.*, 2018, **2**, 024001.

S18. D. Andres-Penares, M. Brotons-Gisbert, C. Bonato, J. F. Sánchez-Royo and B. D. Gerardot, *Appl. Phys. Lett.*, 2021, **119**, 223104.

S19. G. A. Ermolaev, D. V. Grudinin, Y. V. Stebunov, K. V. Voronin, V. G. Kravets, J. Duan, A. B. Mazitov, G. I. Tselikov, A. Bylinkin, D. I. Yakubovsky, S. M. Novikov, D. G. Baranov, A. Y. Nikitin, I. A. Kruglov, T. Shegai, P. Alonso-González, A. N. Grigorenko, A. V. Arsenin, K. S. Novoselov and V. S. Volkov, *Nat. Commun.*, 2021, **12**, 854.

S20. X. Chen, W.-g. Lu, J. Tang, Y. Zhang, Y. Wang, G. D. Scholes and H. Zhong, *Nat. Photonics*, 2021, **15**, 813–816.

S21. C. Wu, T. Wu, X. Jiang, Z. Wang, H. Sha, L. Lin, Z. Lin, Z. Huang, X. Long, M. G. Humphrey and C. Zhang, *J. Am. Chem. Soc.*, 2021, **143**, 4138-4142.

S22. S. Liu, X. Liu, S. Zhao, Y. Liu, L. Li, Q. Ding, Y. Li, Z. Lin, J. Luo and M. Hong,

Angew. Chem., Int. Ed., 2020, **59**, 9414-9417.

S23. Z. Bai, C.-L. Hu, D. Wang, L. Liu, L. Zhang, Y. Huang, F. Yuan and Z. Lin, *Chem. Commun.*, 2020, **56**, 11629-11632.